Check for updates

Received: 31 May 2019 | Revised: 4 August 2019 | Accepted: 5 August 2019

DOI: 10.1002/ppap.201900119

FULL PAPER

PLASMA PROCESSES AND POLYMERS

Development of a model for ultra-precise surface machining of N-BK7® using microwave-driven reactive plasma jet machining

Faezeh Kazemi[1] | **Georg Boehm**[1] | **Thomas Arnold**[1,2]

[1]Department of Precision Surfaces, Leibniz Institute of Surface Engineering (IOM), Leipzig, Germany

[2]Faculty of Mechanical Science and Engineering, Institute of Manufacturing Science and Engineering, Technische Universität Dresden, Dresden, Germany

Correspondence
Faezeh Kazemi, Leibniz Institute of Surface Engineering (IOM), Permoserstraße 15, 04318 Leipzig, Germany.
Email: faezeh.kazemi@iom-leipzig.de

Funding information
German Federal Ministry of Education and Research (BMBF) within the framework of the InnoProfile-Transfer initiative 03IPT706X 'Ultra-precision manufacturing using atomic particle beams'

Abstract

In this paper, extensive studies are conducted as key to overcoming several challenging limitations in applying fluorine-based reactive plasma jet machining (PJM) to surface machining of N-BK7®, particularly regarding the manufacture of freeform optical elements. The chemical composition and lateral distributions of the residual layer are evaluated by X-ray photoelectron spectroscopy and scanning electron microscopy/energy-dispersive X-ray spectroscopy analysis aiming at clarifying the exact chemical kinetics between plasma generated active particles and the N-BK7 surface atoms. Subsequently, a model is developed by performing static etchings to consider the time-varying nonlinearity of the material removal rate and estimate the local etching rate function. Finally, the derived model is extended into the dynamic machining process, and the outcomes are compared with the experimental results.

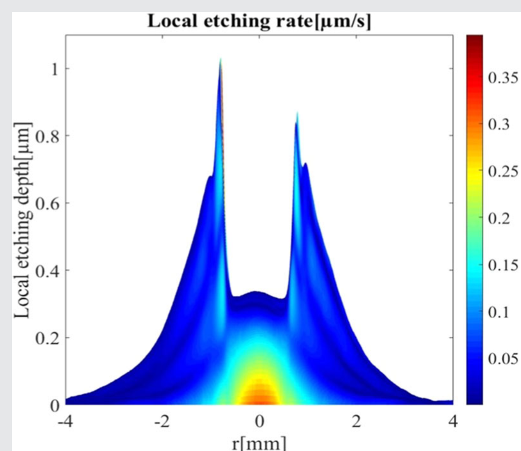

KEYWORDS

modeling, microwave discharges, nonthermal plasma, plasma etching of materials, plasma jet, pulsed discharges

1 | INTRODUCTION

Nowadays, there is a growing demand for optical freeform surfaces for imaging and illumination applications. Such optical elements are beneficial for the construction of compact, light-weight systems that show superior properties compared with conventional systems based on spherical or aspherical elements. As design methods for freeform surfaces are steadily improving, the manufacturing as well as metrology must keep pace. In cases where precise freeform optical elements with individual designs and small lot numbers are needed,

This is an open access article under the terms of the Creative Commons Attribution License, which permits use, distribution and reproduction in any medium, provided the original work is properly cited.

© 2019 The Authors. *Plasma Processes and Polymers* published by Wiley-VCH Verlag GmbH & Co. KGaA

deterministic fabrication methods are required that are capable to shape surfaces with high accuracy and efficiency. Thus, new approaches are necessary to overcome the limitations of classical-mechanical treatments with respect to geometric flexibility and achievable surface shape accuracy as well as production costs and time. Therefore, different types of deterministic surface machining methods such as freeform grinding, computer-controlled polishing, magnetorheological polishing, ion beam figuring, or elastic emission machining have been developed to generate optical components with complex surface shapes.[1–4]

In this context, a local dry etching process based on reactive plasmas and plasma jets was proposed as one step of a process chain for surface form generation and residual topography error correction as an alternative to freeform grinding and subaperture-polishing.[5–13] Such a process chain comprising plasma machining and soft tool polishing has been successfully applied for freeform fabrication of fused silica optical elements.[13] It has been shown, that reactive plasma jet machining (PJM) provides high flexibility regarding the aimed shape, high process convergence, and avoidance of subsurface damage (SSD) due to the chemical nature of material removal. For this technique, a multicomponent nonthermal chemically reactive plasma jet is applied.[14] The active particles, which are created by pulsed microwave power, react with the solid surface and form volatile compounds, and a local dry etching process takes place.[15,16] Etching processes have been used so far mostly for silicon, fused silica, SiC, or ULE® using fluorine-based chemistry, as most of fluoride-silicon compounds are volatile and material removal is achieved in a predictable manner.[17,18]

In this study, we investigate the usage of the PJM technique for borosilicate glass, namely N-BK7® (Edmund Optics company), since this material is even more widely used in optical applications compared to fused silica. However, the application of PJM on this material is not a straightforward approach since N-BK7 contains metal elements such as sodium, barium and potassium, which produce nonvolatile fluorine compounds like BaF_2, NaF, and KF.[19,20] The boiling points of these fluorine compounds are 2260°C, 1704°C, and 1502°C, respectively.[21] Hence, they remain in the solid state on the surface during the process chain of machining, and form a residual layer which covers nonuniformly the plasma treated surface especially at the center of etching zone. The generated residual layer prevents etching and causes roughness on the etched area. To understand the mechanism of residual layer formation during etching, chemical and structural characterization of the layer was performed by XPS and SEM/EDX analysis. It is shown, that the properties of the produced residual layer vary along the plasma treated area, leading to characteristic etching depth profiles. Starting from time dependent local material removal functions obtained from static treatments, the first model for the evolution of dynamic etch profiles is developed and experimentally validated. The results lead to a better understanding of the plasma-surface interaction on N-BK7 and help to develop a predictable machining process for plasma-based freeform generation.

2 | EXPERIMENTAL SECTION

2.1 | Experimental setup

All experiments were carried out in a vacuum test facility consisting of a vacuum chamber with a volume of 0.5 m^3 and a plasma jet system. For the preparation of experiments, the chamber is first evacuated by rotary slide and roots pumps to a minimum pressure of 0.5 mbar. Then, the required process pressure of 900 mbar (i.e., close to the atmospheric pressure) is adjusted via the inlet of N_2 with a manual valve into the recipient and with the aid of a pressure-controlled throttle valve located at the exhaust pipe.

Figure 1 illustrates the plasma jet setup. The plasma jet source is composed of a stainless-steel tube with the exterior diameter of 2 mm and inner diameter of 0.2 mm inserted into the middle of a brass nozzle (with the inner diameter 12 mm). The inserted stainless-steel pipe is fed with 400 sccm helium (He) as an inert carrier gas. Additionally, 1 sccm carbon tetrafluoride (CF_4) and 2 sccm oxygen (O_2) are fed into the tube as the reactive precursor gas mixture to form reactive particles in the plasma jet. Moreover, 400 sccm nitrogen (N_2) is supplied as the inert shielding gas through the exterior brass nozzle to stabilize the gas flow in the plasma jet discharge. All gas feed rates are adjusted by commercially available mass flow controllers (Bronkhorst EL-FLOW).

As can be seen from Figure 1, the gas feeding tubes act as inner and outer electrical conductors of a coaxial system to conduct the microwave energy toward the inner tube outlet. The electric field intensity is provided by a pulsed microwave field at 2.45 GHz for igniting and sustaining plasma at the tip of inner nozzle. The microwave power is generated by a custom-made solid-state generator and is coupled into the plasma source in the form of rectangular pulses by a coaxial cable. For the current investigations, the pulse peak power P_p and the pulse frequency f were set to 200 W and 2.1 kHz, respectively. The pulse width t_p is set to 38 μs to obtain the required mean input power P_M=16 W. The effective microwave power P_E, which is defined as the difference

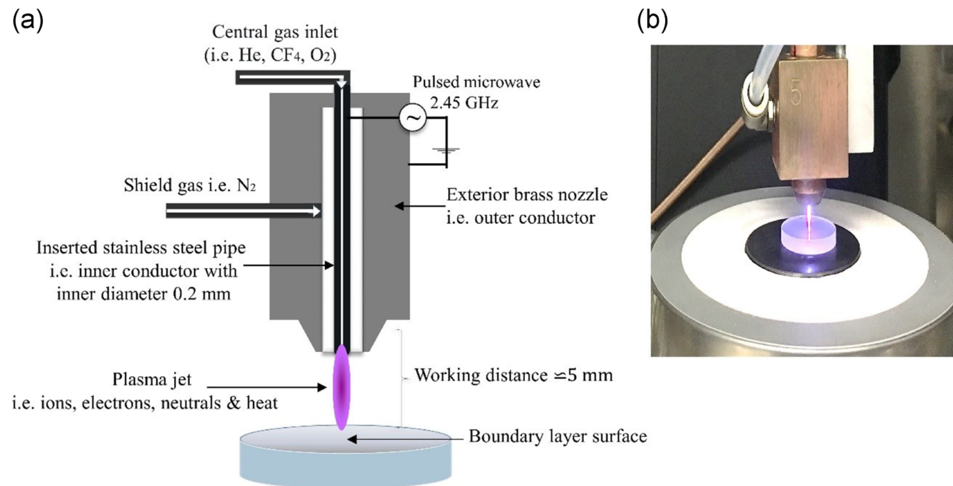

FIGURE 1 (a) Schematic drawing and (b) photograph of the plasma jet interacting with the N-BK7® surface during plasma jet machining process

of mean input power P_M and reflected mean power P_R, was measured by a directional power sensor (Rohde & Schwarz company) located between the microwave generator and the plasma source. The reflected power P_R can be increased or decreased based on the choice of inert carrier gas and depending on tuning the coaxial system. For the experiments, helium plasma with low electron density provides low reflected power P_R, and hence the obtained effective power P_R is practically high, that is, 85%. For the following experiments, the mean input power of 16 W was used, as this setting ensured a stable plasma jet discharge of approximately 8 mm length. Surface temperature during all experiments was determined by IR thermography to be at a constant value of approximately (290 ± 10°C) in the plasma etching zone.

2.2 | Substrate sample preparation

All etching experiments were performed on optically polished N-BK7 wedged windows (Edmund Optics company) with a thickness of 3 mm and diameter of 50 mm. The nominal composition of the initial N-BK7 surface is given in Table 1, according to literature, which was also confirmed by our XPS analysis.[22]

Before the plasma jet treatment, the surfaces of all samples were cleaned carefully by washing in a solution of 1 ml NH_4OH, 2 ml H_2O_2, and 40 ml H_2O and subsequently by a solution of 1 ml HCl, 2 ml H_2O_2, and 8 ml H_2O for 30 minutes at 50°C.

During the plasma processing, residual products remain on the surface of the treated area and are mostly soluble in water/ethanol solution. Therefore, after the plasma processing, the treated surface was rinsed firstly with water/ethanol solution and then cleaned with the above-mentioned solutions. Finally, it was dried in a vacuum drying container. This procedure ensured a precise depth profile measurement on the etched surfaces by optical surface profiler.

2.3 | Measurement and simulation methods

Cross section profiles of etched structures on the N-BK7 surface were determined by using a White Light Interferometer Microscope (NPFLEX-Bruker) where 10 depth profiles were averaged for each structure. Microroughness was measured with a WLI microscope using a 50× objective. The chemical composition of surface was determined by X-ray photoelectron spectroscopy (XPS; instrument Axis Ultra DLD, Kratos Manchester). The surface composition mapping was performed by secondary-electron microscope energy dispersive X-ray (SEM-EDX) measurements in a Zeiss Gemini Ultra 55 machine (Carl Zeiss company) with a Bruker XFlash 3001 detector (Bruker company). The gas flow velocity v_g on the substrate surface was

TABLE 1 Nominal composition of the initial N-BK7® surface[22]

Element	O	Si	C	Na	B	K	Ca	Mg	N	Zn	Ba
Proportion (at.%)	57.9	25.4	4.7	3.9	3.5	3.2	0.5	0.4	0.3	0.2	0.1

estimated over the radial profile r by using COMSOL Multiphysics® (COMSOL Inc. software company), a cross-platform finite element analysis, solver, and Multiphysics simulation software. The simple FEM (Finite Element Method) model was used, which only considered the mass and momentum transfer for the cold Helium gas. For the simulation of depth profiles for dynamic line and area etchings, a MATLAB® script was developed. It allows the calculation of different profile depths for different experimental conditions.

2.4 | Machining methods

For the investigations, three different patterns on the N-BK7 surface were generated, namely the footprint, line, and area etching. The footprint etching forms by a static machining process where the plasma jet dwells on one spot for a certain time. Line and area patterns were created by a dynamic machining process using a moving plasma jet.

For the footprint generation, the plasma jet was placed perpendicular to the substrate surface. Depending on the dwell time t, a footprint with a certain etching depth D is created. It was confirmed by the experiments that the footprint profile has a rotational symmetry, as for instance, the SEM and EDX images obtained from the footprint pattern in static etching of N-BK7 shown in Figure 8. Then, the volumetric removal rate VRR is calculated in terms of the local etching depth $D(r)$ and dwell time t as follows:

$$\mathrm{VRR} = \frac{1}{t}\int_{-\infty}^{+\infty} D(r) 2\pi r \, dr. \tag{1}$$

For achieving a line etching, the plasma jet is horizontally moved by a three-axis motion system relative to the substrate surface while the working distance is fixed. A straight line on the surface is then treated iteratively with the constant scan velocity v resulting in a groove. In this case, the volumetric removal rate VRR is derived by

$$\mathrm{VRR} = \frac{v}{N}\int_{-\infty}^{+\infty} D(x) dx, \tag{2}$$

where N denotes the number of line iterations.

An area etching is performed by moving the plasma jet over the surface in raster path mode. For the experiments, a constant velocity $v = 2$ mm/s and a line feed Δy of 0.1 mm over the surface were used. The working distance was again fixed. An etched area with the desirable size is obtained by adjusting the number and length of lines which are used in

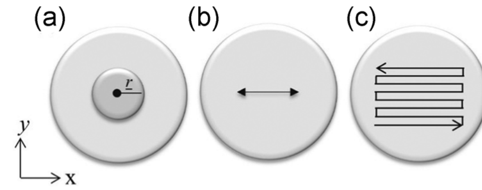

FIGURE 2 Schematics of (a) footprint, (b) line, and (c) area etchings showing the axes definitions and motion directions

the experiment. In this case, the volumetric removal rate VRR is computed as follows:

$$\mathrm{VRR} = v \Delta D \Delta y. \tag{3}$$

For illustrative purpose, the schematics of footprint, line and area etchings showing the axes definitions and motion directions are presented in Figure 2.

3 | RESULTS AND DISCUSSION

3.1 | Optimization of parameters for N-BK7 machining process

Various process parameters affect the fluorine flow densities and consequently the chemical processes in the plasma jet and on the substrate surface. Hence, these parameters have been optimized according to the given application. In this section, the influence of gas mixture and working distance Δd was investigated to improve the efficiency of plasma jet machining of N-BK7. For the following optimization experiments in this section, the line etchings were used at the velocity v =2 mm/s.

3.1.1 | Effect of O_2 addition on etch-profile cross-sections

The dependence of etching depth profiles on the proportion of O_2 in the CF_4/He gas mixture is shown in Figure 3 for the line etchings performed on the N-BK7 surface when the number of iterations $N = 1$ and the working distance Δd = 5mm. For the sake of comparison, the results for fused silica are also provided in the same condition and shown in Figure 3. In these experiments, the flow rates of CF_4, He, and N_2 were fixed to the constant values 1, 400, and 400 sccm, respectively, while the O_2 flow rate was increased from 0 sccm to 4 sccm. One can observe from Figure 3 that the etching profiles exhibit nearly a Gaussian shape except the ones with the low O_2 rate (i.e., when it is <2 sccm for N-BK7 and it is <1 sccm for fused silica) where nearly no etching in the center of the profile is achieved. However, at lateral

FIGURE 3 Etch-profile depth of (a) N-BK7® and (b) fused silica; and (c) the corresponding volumetric removal rate volumetric removal rate (VRR) depending on the O_2 gas flow rate

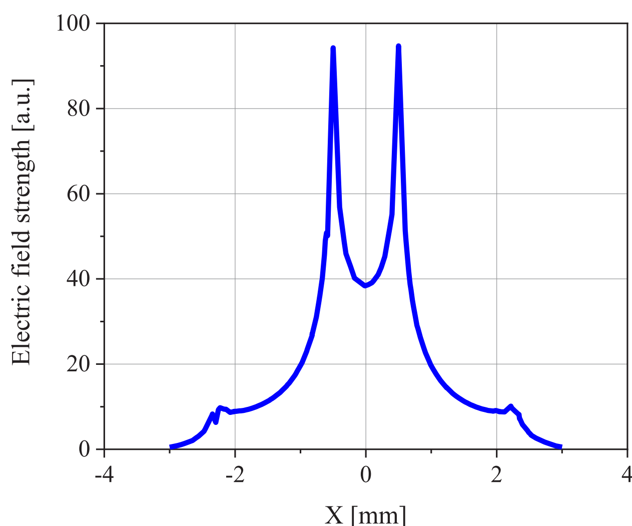

FIGURE 4 Cross-section of electric field strength at inner gas tube outlet of the plasma jet source calculated by FEM (Finite Element Method)

positions, a similar etching as for higher O_2 flow rates is observed for both N-BK7 and fused silica.

It is assumed that the dissociation of CF_4 generating fluorine atoms or F^- ions preferably takes place in the region of high electric field strength. A simple FEM model simulating the electric field distribution of the coaxial conductor system was used with no ignited plasma discharge. The FEM simulation of electric field strength at the inner conductor in Figure 4 validates this assumption by showing an annular shaped region of maximum field strength that occurs at the edges of the inner nozzle. In the center region where high CF_4 concentration and lower electric field strength occurs, the CF_x radical formation is more probable. It is known that CF_x radicals generated in fluorocarbon plasmas by electron impact dissociation can lead to the deposition of a fluorocarbon film on the surface.[23] Obviously, a masking layer is formed in the center during the treatment that inhibits the fluorine radical attack. The deposition rate of

fluorocarbon film depends on the gas composition and precursor density. In the case where no O_2 is added into the gas mixture or the O_2 flow rate is low, the fluorocarbon film deposits fast on the surface. Then, the film continues to thicken and makes the attained local etch rates in the center nearly negligible.

However, it is well-known that oxygen has the capability of reacting with neutral CF_x to form COF_2 and F_2.[24] By increasing the O_2 content in the gas mixture, not only the deposition rate of the fluorocarbon film on the surface is impaired but also a larger concentration of F atoms or F^- ions is provided for etching the surface, and hence the etching rate in the center of the plasma interaction zone increases.[24,25] On the other hand, the addition of O_2 to the gas mixture leads to dispersing the plasma energy discharge since O_2 molecules compete with CF_4 molecules in energy uptake from the free electrons in the plasma discharge leading to excited states, dissociation, or formation of ions.

Furthermore, a dilution of the fluorine radical concentration becomes effective. Hence, the etching rate decreases for N-BK7® and fused silica, respectively, when the O_2 flow rate exceeds from 2 sccm and 1 sccm. A similar behavior of adding O_2 has been reported by Mogab et al.[26] in the case of a low-pressure CF_4-O_2 plasma etching process. For the following experiments on the plasma jet machining of N-BK7®, the optimal flow rate of O_2 was adjusted to 2 sccm.

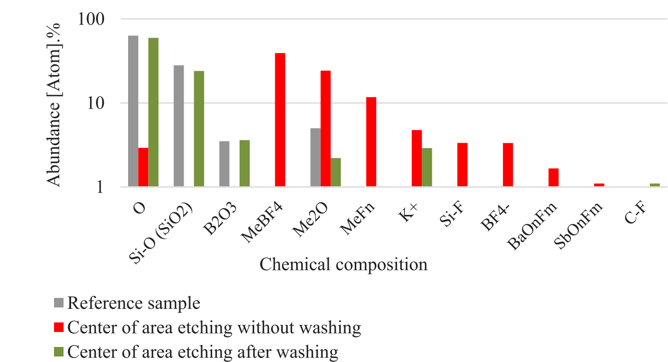

FIGURE 6 Chemical composition of N-BK7® surface measured by XPS before, after area etching, and after removal of the residual layer where Me can stand for Na, K, and Ba

3.1.2 | Effect of working distance Δd on etch-profile cross-sections

The active region of plasma discharge and consequently the etch efficiency of the plasma jet for both dynamic and static surface machining strongly depend on the distance between the plasma jet outlet and substrate surface (i.e., working distance Δd). The dependence of working distance on the etching depth D is investigated for the line etching with the number of iterations $N = 2$. Figure 5 shows the cross-section profiles at different working distances Δd. At $\Delta d = 5$ mm the material removal rate reaches a maximum. It is assumed that the generation of etching particles such as fluorine radicals is promoted by oxygen entrainment from the peripheral gas flow, yielding optimal conditions for dissociation of CF_4 and oxidation to COF_2 preventing the recombination of fluorine radicals. For a larger working distance, recombination effects may become stronger. In the following experiments, the working distance was set to 5 mm.

3.2 | Surface characterization of plasma-treated N-BK7

To investigate the chemical composition of nonvolatile compounds formed on the surface after plasma jet etching, a raster path scheme was applied, as described in Section 2.4. The process parameters were adjusted to the optimum parameters determined in the previous

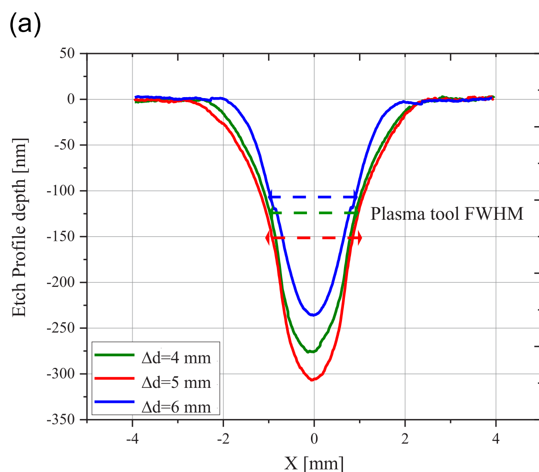

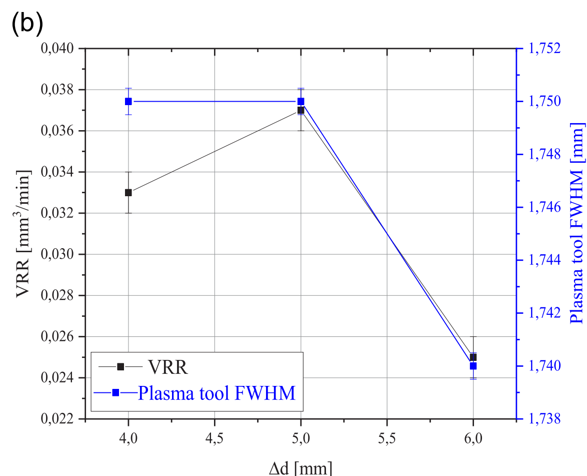

FIGURE 5 (a) Etch profile depth, and (b) volumetric removal rate (VRR) as well as the plasma tool FWHM depending on the working distance Δd

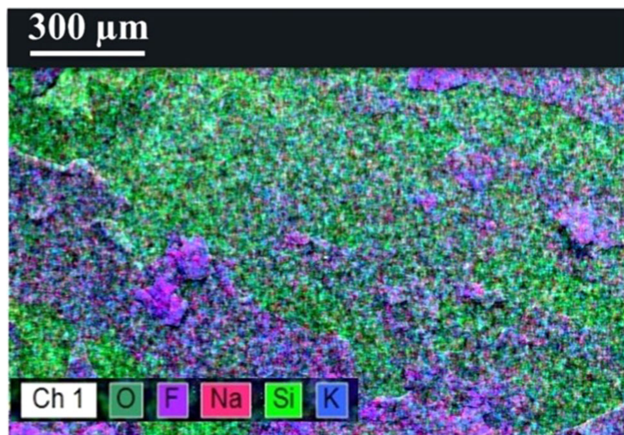

FIGURE 7 Energy dispersive x-ray analysis image of residual layer, which forms on the plasma treated surface of N-BK7® after area etching

experiments (i.e., $P_M = 16W$, $\Delta d = 5\,mm$, $CF_4 = 1\,sccm$, $O_2 = 2\,sccm$, $He = 400\,sccm$, $N_2 = 400\,sccm$).

After the plasma processing, a rough residual layer forms on the plasma affected area, which was analyzed by XPS. For reference, the chemical composition of an unprocessed N-BK7 surface was measured and the amount of the components was determined in atom.%. The result is depicted in Figure 6 as reference. In addition, the chemical composition of the N-BK7 surface after etching is presented in the same figure, where the measurement results directly after plasma processing and after a subsequent water/ethanol cleaning process, respectively, are shown. It can be observed that the residual layer formed on the plasma treated surface consists of a variety of metal oxides and fluorides such as Na_2O, NaF, KF, BaF_2, and multielement compounds like BaO_nF_m, BaF_6S, and SbO_nF_m(s) as well as a fluoridic B compound (BF_4^-). The XPS analysis after washing exhibits a surface with very low amount of residual etching products.

The chemical and structural properties of the plasma treated area was further investigated by imaging EDX analysis. Figure 7 shows the result directly after the plasma treatment before washing. A nonuniform distribution of Na/F and K/F signals assigned to the formed residues NaF and KF, and Si/O signals with weak homogeneously distributed Na and K signals assigned to the substrate material N-BK7 is observed. Due to the inhomogeneous coverage of the surface by the residuals, layer thickness determination could not be performed.

The XPS and EDX results indicate that the reactions of N-BK7 surface in interaction with the $He/CF_4/O_2$-based plasma can be described into two general categories. One includes reactions between fluorine and network formers, that is, 70% silica (SiO_2) and 8% boron trioxide (B_2O_3). The other category entails the interaction between fluorine and the metal oxides (i.e., BaO, K_2O, and Na_2O). The reactions of the first category produce volatile compounds such as SiF_4(g), CO(g), CO_2(g), BF_3(g), B_2F_4(g), and COF_2, which have very low boiling points (see Table 2).[27] The desorption of these volatile compounds from the surface occurs by thermal activation, which results in material removal. In contrast, the second category of reactions forms nonvolatile fluorine compounds such as NaF, KF, BaF_2 as well as the multielements' layer like BaO_nF_m and SbO_nF_m that remain on the surface.

3.2.1 | Local distribution of residual layer

Area etchings yield limited information on the local interaction of the plasma jet with the surface. This is due to the fact that the relative motion of the plasma jet leads to the convolution of the local removal function $R(x, y)$ with the plasma dwell time t at certain coordinates x, y in the Cartesian coordinate system. Then, the local etching depth $D(x, y)$ is determined as follows:[13]

$$D(x,y) = \iint R(x-\bar{x}, y-\bar{y}) \cdot t(\bar{x},\bar{y}) d\bar{x} d\bar{y} \quad (4)$$

Therefore, static footprint etchings have been performed to investigate simply the local depth and the lateral distributions of the residuals. Figures 8 and 9 show the SEM images of a footprint obtained for an etching time of $t=8$ s. The formation of a residual layer is clearly seen. In the central area with a radius of approximately 400 µm, the layer is cracked into several patches and partly delaminated. At the peripheral area, the layer seems to be compact until the edge at r ~800 µm, where the layer is fully delaminated in a ring-like zone. However, at an even larger radius (i.e.,

TABLE 2 Boiling points (BP) and vapor pressure of volatile and nonvolatile components of N-BK7® surface in interaction with CF_4/O_2-based plasma discharge[27]

Reaction product	CO	BF_3	SiF_4	COF_2	CO_2	KF	NaF	BaF_2
Boiling point (°C)	−191	−100	−86	−84	−78	1,505	1,700	2,260
Vapor pressure	34 [atm] (−140°C)	>50 [atm] (20°C)	36.5 [atm] (20°C)	55.4 [atm] (20°C)	56.5 [atm] (20°C)	0.0013 [atm] (885°C)	0.0013 [atm] (1,077°C)	0.0013 [atm] (1,436°C)

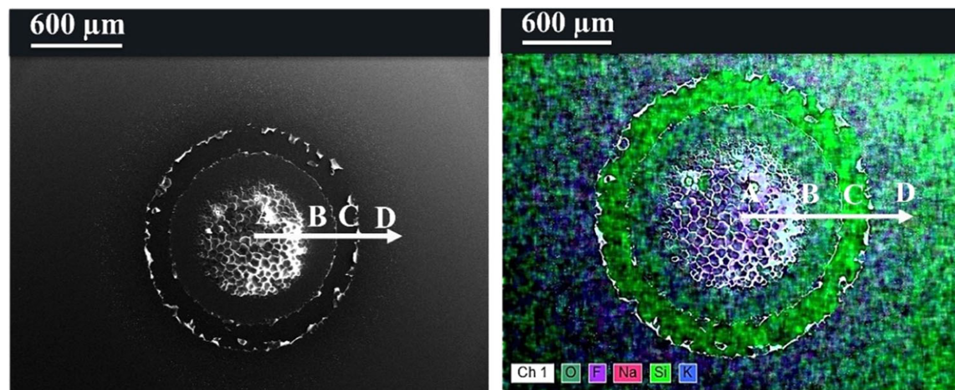

FIGURE 8 Scanning electron microscopy (left) and energy dispersive x-ray (right) images of a footprint obtained after static etching for an etching time of $t = 8$ s

$r > 800 \mu m$), a compact layer is again visible, though partly delaminated on the edge. This finding is consistent with the EDX measurement shown in Figure 8, where the main components of the substrate and residuals are color-coded.

Four different spots (labeled with A, B, C, D) along the radial profile r have been further analyzed to reveal their corresponding chemical composition. The relative abundance of elements at those spots is shown in Figure 10. At the center of the footprint pattern (i.e., the location A), the largest amount of fluorine as well as Na and K is measured. This is attributed to the residual layer consisting of NaF and KF with the largest thickness that accumulates at the center of the footprint. At position B, the signal indicating alkali-fluorides decreases, while at the position C approximately 0.8 mm distance from the center, nearly no fluorine occurs, and the Si and O signal

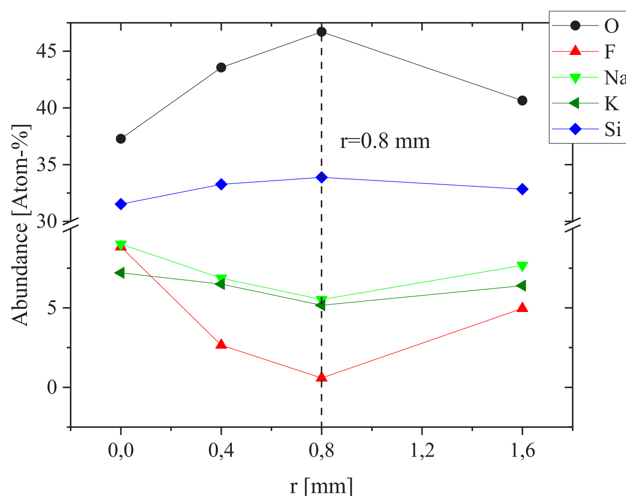

FIGURE 10 Relative abundance of elements at the spots shown in Figure 8 with the labels A, B, C, D

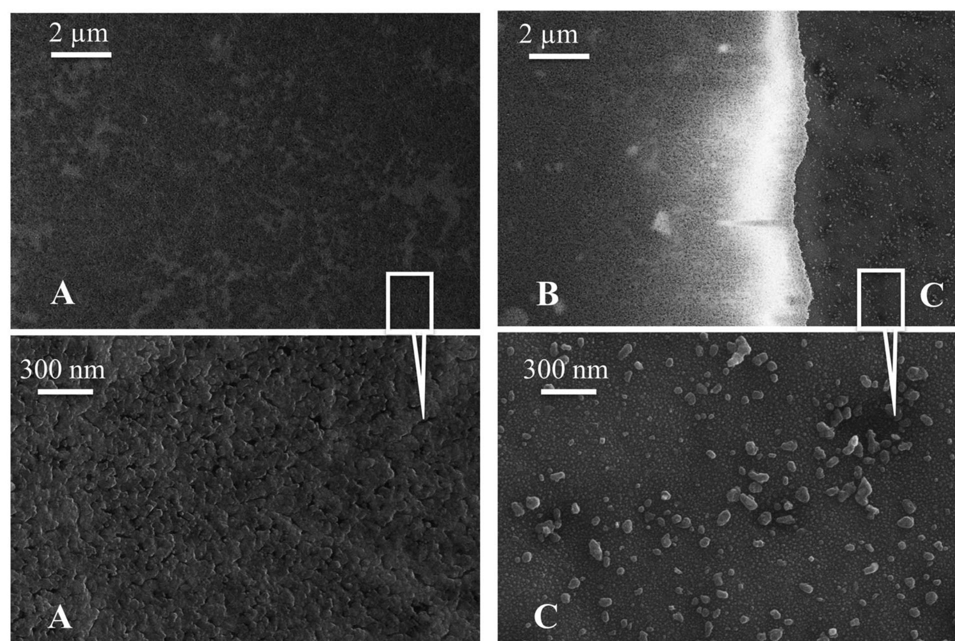

FIGURE 9 Surface morphology scanning electron microscopy of the spots A, B, C corresponding to Figure8

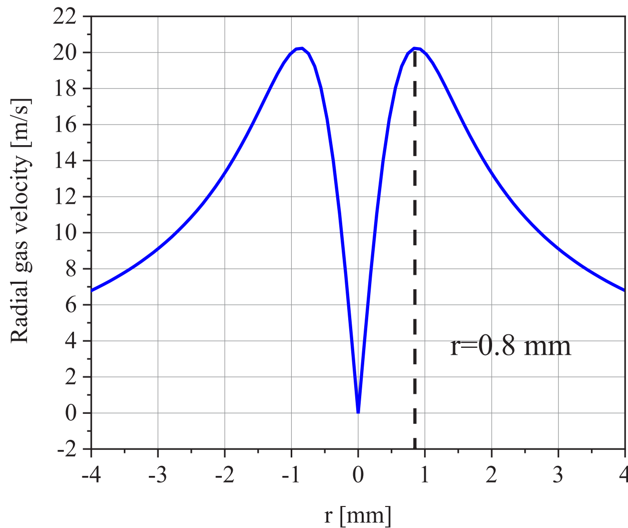

FIGURE 11 Velocity magnitude of radial gas flow for He gas jet at $z = 5$ mm on a perpendicular plate

exhibit a maximum. According to the SEM images in Figures 8 and 9, the residual layer is removed at this radial position and the initial N-BK7 surface appears.

This radial distribution of the residual layer can be explained by the gas flow pattern of the plasma jet. In this configuration, an impinging jet flow is assumed that forms a stagnation point in the center. A FEM simulation of a helium jet emerging from a tube with the inner diameter of 0.2 mm, that is directed to a perpendicular plate at the distance of 5 mm, was performed to obtain the radial gas velocity on the plate surface (i.e., the velocity component parallel to the surface).

The distribution of radial gas flow velocity is shown in Figure 11. At the radial position of 0.8 mm approximately, the maximum is observed. As the residual layer

is probably not compact and prone to delaminate, the gas blows loose parts outwards and spreads it radially over the surface. In the SEM image, such particles are found around the footprint.

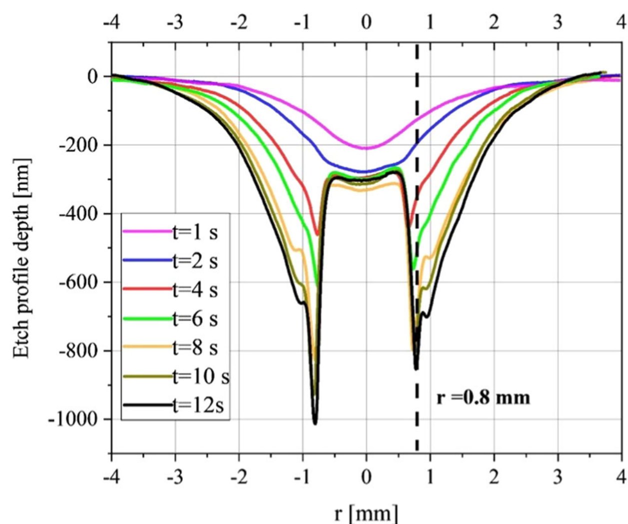

FIGURE 12 Etch-profile depth obtained by reactive plasma jet on N-BK7® surface after static plasma processing and removal of the residual layer with water/ethanol solution

3.2.2 | Etch profile as a function of dwell time

Static etching for different treatment times t was performed to investigate the temporal evolution of etch profiles. Figure 12 depicts the cross-section of etching profiles for the dwell times of 1 to 12 s. Note that the profiles shown in Figure 12 were measured after removing the residual layer by washing at the end of experiments.

At the beginning of the process when the dwell time t is <2 s, the profiles exhibit a near-Gaussian shape, that is usually found for fused silica or Si plasma jet etching.[14] Hence, the near-Gaussian profile represents the reactive particle density distribution always present on the surface. Even if a residual layer is formed, it is thin enough to be penetrated by etching species and the isotropic etching can proceed. However, as the dwell time increases, the profiles depart significantly from the Gaussian shape. Obviously, the residual layer in the center is masking the surface underneath and prevents the attack of etching species. Thus, etching is inhibited leading to a flattened profile shape. Consequently, by increasing the etching time t, material removal is barely observed at the center and the local etching rate R is reduced considerably. Contrariwise, the gas velocity v_g at the radial position of 0.8 mm reaches a maximum (e.g., 20 m/s; see Figure 11) such that the brittle residual layer is cracked easily and blown away by the gas flow, and the parted residual particles stay on the surface instead of a dense residual layer. Therefore, the profile cross sections show a sharp edge at $r > 0.8$ mm because the local material removal is not affected by the separated residual particles dispersed over the surface.

The SEM image for the peripheral area of the footprint at the etching time $t = 8$ s before washing and cleaning is shown in Figure 9 (the spot C) at the Section 3.2.

3.2.3 | Roughness measurement

After washing the plasma treated sample, the roughness of footprint etching over the radial profile r was determined. Figure 13 illustrates a qualitative dependence of N-BK7 surface roughness on the etching time t ranging from 1 s to 8 s for 21 different spots on the radial profile. At the beginning of footprint etching when the

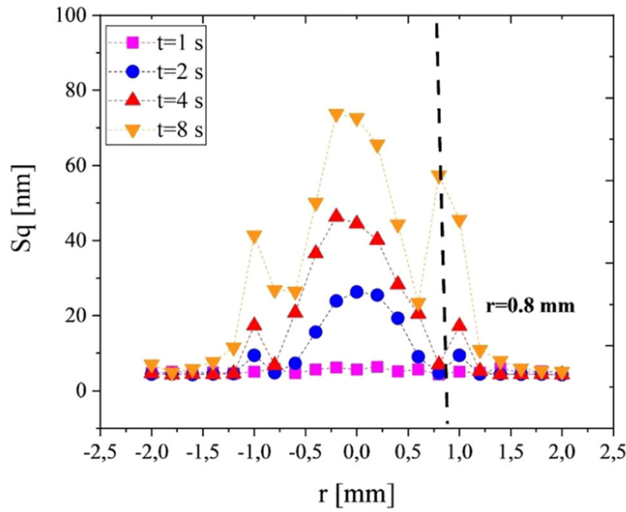

FIGURE 13 Surface roughness of N-BK7® which forms after static etching at different etching times t for 21 different spots of radial profile

etching time t is <2 s, the etching results in a relatively smooth surface, and the measured roughness of footprint (i.e., Sq = 4 nm) does not change remarkably in comparison to the polished N-BK7 surface without any plasma treatment (Figure 13, the curve at $t = 1$ s). However, by increasing the etching time t, the measured roughness over the radial profile r rises especially at the center and at approximately $r = 0.8$ mm. At the center, the thick local residual layer converts into a masking layer during the process. However, as it seems to partly delaminate, the mask is not fully dense, and it leads to a rough surface.

Additionally, at the peripheral area of footprint, the brittle residual layer is locally cracked and removed during the process by increasing the etching time. However, the separated residual particles instead of a dense and packed residual layer remain on the surface, and cause a rough surface (Figure 9, the spot C).

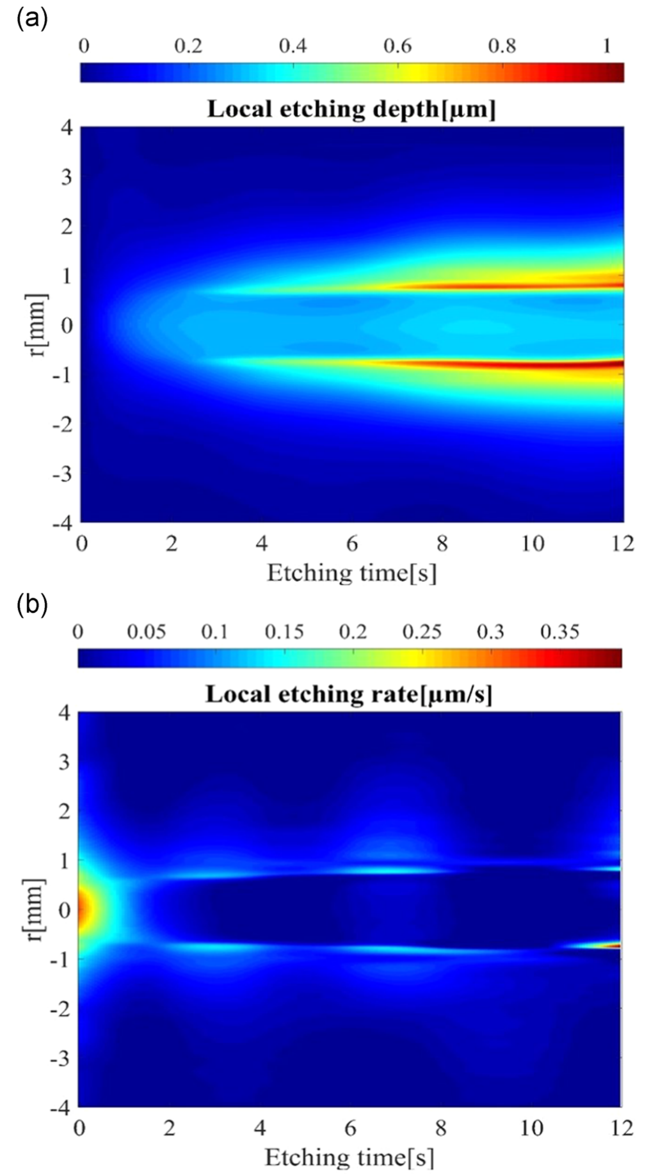

FIGURE 14 (a) The attainable local etching depth D of static machining for N-BK7® as a function of the radial profile r and etching time t; (b) the corresponding local etching rate R based on the obtained depth D over the radial profile r and etching time t

3.2.4 | Estimation of local etching rate R

The experimental data presented in Figure 12 is used to illustrate the depth D of static etching for N-BK7 as a function of the radial profile r and etching time t (see Figure 14). For conventional deterministic machining in which the local etching rate $R(r)$ is constant with respect to the etching time t, we can simply write the relation between the local etching rate $R(r)$ and the depth D as

$$R(r) = \frac{D(r)}{t}, \tag{5}$$

However, as discussed before, the removal behavior of N-BK7 is not linear in terms of etching time t. Hence, to compute the local etching rate R of N-BK7, the etching time t must be considered as an extra variable in addition to the radial position r. In this case, the relation between the local etching rate R and the depth D is expressed as follows:

$$R(r, t) = \frac{\partial D(r, t)}{\partial t}. \tag{6}$$

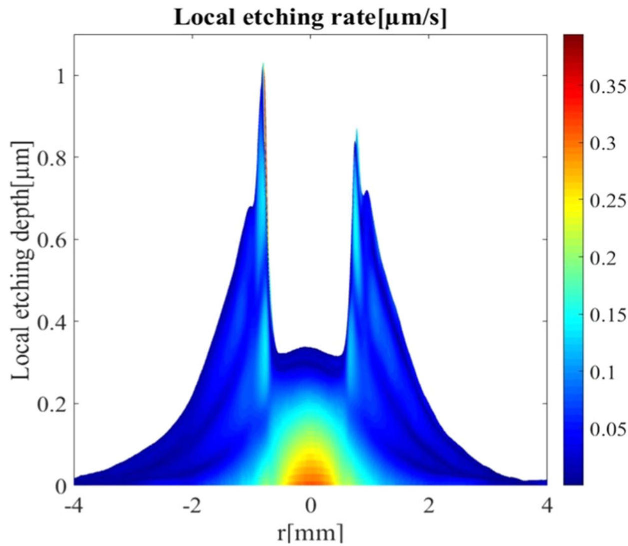

FIGURE 15 Interpolant of local etching rate R in terms of the etching depth D and radius r

According to Equation (6), the local etching rate $R(r, t)$ is computed by the partial derivative of depth $D(r, t)$ with respect to the etching time t. The experimental data has been interpolated to obtain a smooth 2-dimensional function R, that is shown in Figure 14a. The result of the local etching rate is illustrated in Figure 14b.

Based on this function, it is now possible to calculate a dependence of the rate on the already reached etching depth $D(r, t)$ for a certain radius, i.e., $R(D(r, t), r)$. By using an interpolation routine, a new data set for $R(D(r, t), r)$ is generated, which is shown in Figure 15. We can observe from Figure 15 that the local etching rate R is maximum at the center of radial profile r where the depth is low e.g., $D < 0.2$ μm. However, the etching rate R decreases and approaches zero with some small fluctuations in its amount as the depth D increases. These fluctuations of local etching rate R at the center for large values of depth D can be attributed to the brittle residual layer on the surface which can be removed coincidentally by the gas flow velocity v_g during the process.

The peaks in depth D are achieved for the radial profile around $r = -0.8$ and $r = 1$ mm as the gas flow velocity v_g has the highest amount (see Figure 11) and results in the removal of the residual layer. In the following, the local etching rate function is used for simulation of a dynamic line etching.

3.2.5 | Simulation of dynamic surface machining

The simulation algorithm assumes an etching rate function $R(D(x - x_c, y - y_c, t))$ in 2D coordinate space, where x_c and y_c denote the center-point of the rate function. The motion is implemented by the iterative shifting $x_c(t)$ in the case of a line etching, or $x_c(t)$ and $y_c(t)$ in the case of area etching according to the applied velocity and direction. The starting etching depth is initialized to $D(x, y, t_0) = 0$. Further etching is then realized by accumulating $D = D + dD$, where $dD = R\,dt$, and dt is the time step. Table 3 summarizes the proposed algorithm. The algorithm described in Table 3 is implemented in MATLAB®, and the

TABLE 3 Proposed algorithm for creating the dynamic surface machining from the footprint profile that is already obtained using the static process

Algorithm 1
Require: Simulation of dynamic surface machining
Input: Experimental static footprint etching
Output: Simulated line and area etching
1. Initialization:
(a) Define 2D space over x and y axes
(b) Set the center of footprint for $t = t_0$ at $x_c(t_0) = x_0$ and $y_c(t_0) = y_0$
(c) Set the principal etching depth $D(x_0, y_0) = 0$
(d) Set the masking constrains $R_0 = 0, D_0 > 0.3$μm, $r_0 < 0.5$mm
2. While $i \leq I - 1$ where I denotes the total number of time steps for the given maximum etching time $t = t_{max}$:
(a) Calculate the radial profile $r(t_i) = \sqrt{(x - x_c(t_i))^2 + (y - y_c(t_i))^2}$
where $t_i = t_0 + i\Delta t$ denotes the current etching time and Δt is the time-step
(b) Calculate the interpolant of the local etching rate $R(D(r(t_i), t_i), r(t_i))$
(c) **If:** $R(D(t_i), r(t_i)) = R_0 = 0$ and $D(r(t_i), t_i) > D_0$ where $r(t_i) < r_0$, then a mask is made by stopping the etching, i.e., $D((r(t_{i+1}), t_{i+1})) = D(r(t_i), t_i)$
(d) **Else:** Perform the etching by calculating the new depth D as
$D((r(t_{i+1}), t_{i+1})) = D(r(t_i), t_i) + \Delta t R(D(t_i), r(t_i))$
(e) Move the center point of etching profile by
$x_c(t_{i+1}) = x_c(t_i) - (-1^n v\Delta t)$
$y_c(t_{i+1}) = y_c(t_i)$
where n denotes the etching iteration index and v is the velocity in mm/s
3. If: line etching
(a) Reset the center point as $x_c(t_0) \rightarrow x_c(t_{N-1})$ and $y_c(t_0) \rightarrow y_0$
(b) Go to the step 2 for the next etching iteration $n \rightarrow n + 1$
4. Else If: area etching
(a) Reset the center point as $x_c(t_0) \rightarrow x_c(t_{N-1})$ and $y_c(t_0) \rightarrow y_c(t_0) + \Delta y$ where Δy denotes the line feed in mm
(b) Go to the step 2 for the next etching iteration $n \rightarrow n + 1$

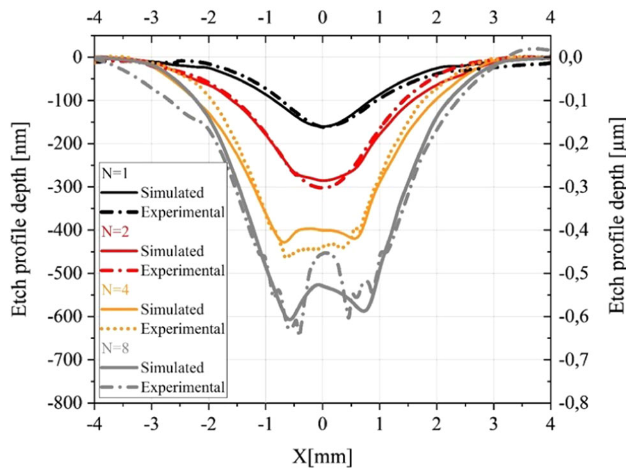

FIGURE 16 Etch profile depth obtained by the experimental approach and the proposed simulation algorithm for line etching on the N-BK7® surface with different numbers of line iterations N

simulation results are obtained for both the line and area etching. Figure 16 shows the cross-sectional shape of simulated depth profiles and experimental results for the line etching. It can be observed that the calculated profiles agree well with the experimental results for the same setting parameters when the velocity $v = 2$ mm/s is used and the number of line iterations N is set to $\{1, 2, 4, 8\}$.

Furthermore, Figure 17a,b, respectively, show the simulated and experimental results for the case of area etching when the velocity $v = 4$ mm/s is used, the line feed Δy is 0.1 mm and the number of etching iterations N is 70. In addition, the cross-sectional shape of etched area for both the simulated and experimental results is presented in Figure 17c,d.

It can be observed that the simulated cross section matches with the experimental etch profile. Both the experimental and simulated profile exhibit a complex shape (see Figure 17). Obviously, the produced residual layer in the center of the etching zone reduces the removal depth. At the beginning of area etching, this dense layer reduces the diffusion of fluorine atoms into the surface of N-BK7 repeatedly and causes the ripple-structure at a position of $x = -4$mm. The same effect causes the ripple structures at the beginning and end of the cross-section profile in the y-direction.

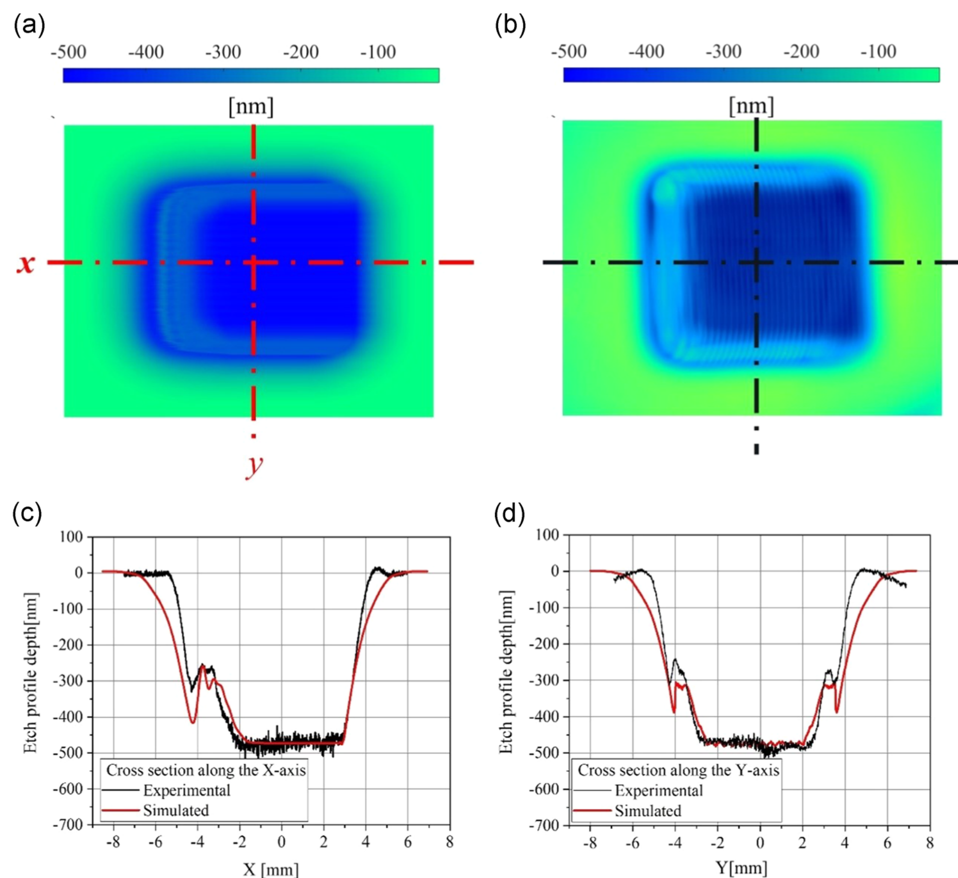

FIGURE 17 Area etching results: (a) the outcome of the proposed simulation algorithm and (b) the experimental results when the velocity $v = 4$ mm/s is used; Cross-sectional shape of area etching: (c) along the x-axis and (d) along the y-axis where the red line indicates the simulation results, and the black line indicates experimental results

4 | CONCLUSION

This paper describes comprehensive investigations on the surface machining of N-BK7 with fluorine-based microwave-driven PJM. The plasma generates active particles that chemically react with the N-BK7 surface to create both volatile and nonvolatile compounds. Based on previous research studies, the surface machining process of N-BK7 relies on the generation of volatile compounds such as $SiF_4(g)$, $CO(g)$, $CO_2(g)$, $BF_3(g)$, $B_2F_4(g)$, and COF_2, which convert the solid substrate surface to gaseous compounds.[27] The desorption of these volatile compounds from the N-BK7 surface occurs spontaneously by a thermal activation, which results in the etched surface. However, nonvolatile compounds form a residual layer on the surface which changes the typical Gaussian-like etch profile and subsequently causes the reduction and nonlinearity in the material removal rate.

Based on the XPS and EDX/SEM analysis of the plasma-treated surface of N-BK7, it was shown that the residual layer consists of a variety of nonvolatile metal oxides and fluorides such as Na_2O, NaF, KF, BaF_2, and multielement compounds like BaO_nF_m, BaF_6S, and $SbO_nF_m(s)$ as well as a fluoridic B compound (BF_4^-). However, the XPS analysis also proved that most of these residual etching products are washable by the water/ethanol solution and can be removed.

Furthermore, the mechanism between plasma generated active particles and the N-BK7 surface atoms was described by evaluating lateral distributions of residual layer during the static footprint etching.

The static footprint etching for different treatment times was performed to monitor the temporal evolution of the etch profile depth. At the beginning of the process, although the residual layer is formed, it is thin enough to be penetrated by etching particles, and the isotropic etching can be continued. However, as the treatment time increases, the residual layer masks the surface underneath and prevents the attack of etching species. Thus, etching is inhibited leading to a flattened profile shape. Subsequently, the local etching rate was modeled over the radial profile to account for the time-varying nonlinearity of the material removal rate. It was observed that the local etching rate decreases disparately over the radial profile such that the highest local etching rate drop is measured at the center. By using the temporal local etching rate function, a model was established that is capable to simulate dynamic etching, such as line and area etching of N-BK7. This model is a prerequisite for a deterministic etching process employing dwell time simulation algorithms. To predict etching depths for varying dwell times, these algorithms have to take into account the complex tool function behavior.

It is concluded from our investigations that generally fluorine-based PJM can be applied for shape generation and error correction of freeform optics of N-BK7. By introducing a model that is capable of simulation, the results of this study help to establish a plasma-based process chain for shape generation and error correction of N-BK7 freeform optics. As it turned out that the surface roughness is not sufficient for freeform optical application, the process chain should comprise additional polishing steps, for example, shape preserving bonnet polishing.

However, there is still need for improvement and further research on the N-BK7 surface machining procedure with fluorine-based PJM. The aspects of higher surface temperatures and larger mean input powers are subjects for future work.

ACKNOWLEDGEMENTS

The authors would like also to thank Dr. J. Bauer, D. Hirsch, and T. Liebeskind for supplying the measurement system. Financial support by German Federal Ministry of Education and Research (BMBF) within the framework of the InnoProfile-Transfer initiative 03IPT706X 'Ultra-precision manufacturing using atomic particle beams' is gratefully acknowledged.

ORCID

Faezeh Kazemi http://orcid.org/0000-0003-2974-0726

REFERENCES

[1] D. Walker, G. Y. Yu, C. Gray, P. Rees, M. Bibby, H. Y. Wu, X. Zheng, *Adv. Mater. Res.* **2016**, *1136*, 684.
[2] J. A. Menapace, P. J. Davis, W. A. Steele, M. R. Hachkowski, A. Nelson, K. Xin, *Proc. SPIE* **2007**, *6403*, 64030N.
[3] T. Kamimura, S. Fukumoto, R. Ono, Y. K. Yap, M. Yoshimura, Y. Mori, T. Sasaki, K. Yoshida, *Opt. Lett.* **2002**, *27*, 616.
[4] Y. Mori, K. Yamauchi, K. Endo, *Precis. Eng.* **1987**, *9*, 123.
[5] H. Takino, N. Shibata, H. Itoh, T. Kobayashi, H. Tanaka, M. Ebi, K. Yamamura, Y. Sano, Y. Mori, *Appl. Opt.* **1998**, *37*, 5198.
[6] Y. Mori, K. Yamamura, Y. Sano, presented at 9th ICPE, Japan, August 29-September 1, 1999.
[7] H. Takino, N. S hibata, T. Kobayashi, H. Itoh, H. Tanaka, A. Koike, K. Nakano, K. Yamamura, Y. Sano, Y. Mori, presented at 9th ICPE, Japan, August 29-September 1, 1999.
[8] H. Takino, N. Shibata, H. Itoh, T. Kobayashi, K. Yamamura, Y. Sano, Y. Mori, *Appl. Opt.* **2002**, *41*, 3971.
[9] A. Schindler, G. Boehm, T. Haensel, W. Frank, A. Nickel et al., *Proc. SPIE 4451* **2001**, 242.

[10] T. Arnold, G. Boehm, A. Schindler, *J. Vac. Sci. Technol.* **2001**, *A 19*, 2586.
[11] T. Arnold, G. Böhm, H. Paetzelt, *Contrib. Plasm. Phys.* **2014**, *54*, 145.
[12] H. Paetzelt, G. Böhm, T. Arnold, *Plasma Sources Sci. Technol.* **2015**, *24*, 025002.
[13] T. Arnold, G. Boehm, H. Paetzelt, H. Paetzelt, *J. Eur. Opt. Soc.-Rapid* **2016**, *11*, 16002.
[14] P. Piechulla, J. Bauer, G. Boehm, H. Paetzelt, T. Arnold, *Plasma Process. Polym.* **2016**, *13*, 1128.
[15] V. M. Donnelly, A. Kornblit, *J. Vacuum Sci. Tech. A* **2013**, *31*, 050825.
[16] H. Paetzelt, G. Böhm, T. Arnold, *Plasma Sources Sci. Technol.* **2015**, *24*, 025002.
[17] M. Castelli, R. Jourdain, P. Morantz, P. Shore, *Precis. Eng.* **2012**, *36*, 467.
[18] Z. Dai, X. Xie, H. Chen, L. Zhou, *Plasma Chem. Plasma Process.* **2018**, *38*, 443.
[19] C. Constantine, *Micromach. Dev.* **1997**, *12*, 2.
[20] P. W. Leech, *Vacuum* **1999**, *55*, 191.
[21] T. Ichiki, Y. Sugiyama, T. Ujiie, Y. Horiike, *J. Vacuum Sci. Tech. B* **2003**, *21*, 2188.
[22] H. Kreilkamp, Analyse der Einflüsse auf die Gestaltabweichung gepresster Glasoptiken beim nicht-isothermen Blankpressen, Apprimus Verlag, Aachen, Deutschland, 2018.
[23] A. Sankaran, M. J. Kushner, *J. Appl. Phys.* **2003**, *82*, 1824.
[24] A. Fridman, *Plasma Chemistry*, Cambridge University Press, Cambridge, UK **2008**.
[25] C. I. M. Beenakker, J. H. J. van Dommelen, R. P. J. van de Poll, *J. Appl. Phys.* **1981**, *52*, 480.
[26] C. J. Mogab, A. C. Adams, D. L. Flamm, *J. Appl. Phys.* **1978**, *49*, 3796.
[27] a) J. Schmitt, A. Meier, U. Wallrabe, F. Voelklein, *Int. J. Glass. Sci* **2018**, *9*, 499; b)National Institute of Standards and Technology, NIST Standard Reference Database, https://webbook.nist.gov/chemistry/ (accessed: October 2018).

How to cite this article: Kazemi F, Boehm G, Arnold T. Development of a model for ultra-precise surface machining of N-BK7® using microwave-driven reactive plasma jet machining. *Plasma Process Polym*. 2019;16:1900119. https://doi.org/10.1002/ppap.201900119